Soft Matter

Assembly of Nanocrystal Clusters by Solvent Evaporation: Icosahe- dral Order and the Breakdown of the Maxwell Regime

Journal:	*Soft Matter*
Manuscript ID	SM-ART-05-2020-000838.R1
Article Type:	Paper
Date Submitted by the Author:	04-Jun-2020
Complete List of Authors:	Macias, Elizabeth; Iowa State University of Science and Technology, Physics and Astronomy Waltmann, Thomas; University of Michigan, Physics Travesset, Alex; Iowa State University of Science and Technology, Physics and Astronomy

Soft Matter

ARTICLE TYPE

Cite this: DOI: 00.0000/xxxxxxxxxx

Assembly of Nanocrystal Clusters by Solvent Evaporation: Icosahedral Order and the Breakdown of the Maxwell Regime

Elizabeth Macias, Tommy Waltmann, and Alex Travesset

Received Date
Accepted Date

DOI: 00.0000/xxxxxxxxxx

We carry molecular dynamics simulations of N gold alkylthiolated nanocrystals ($0 \leq N \leq 29$) contained in liquid droplets of octane, nonane and decane coexisting with its vapor. The equilibrium structures that result when all the solvent dries up consist of highly symmetric nanocrystal clusters with different degrees of icosahedral order that are thoroughly characterized. We show that the relaxation times follows two regimes, a first for small nanocrystal packing fraction, dominated by the diffusion of vapor molecules (Maxwell regime, relaxation times independent of N) and another, for larger packing fractions, where the solvent diffuses through the cluster (with relaxation times growing like $N^{2/3}$). We discuss the connection to the assembly of superlattices, prediction of lattice constants and evaporation models.

1 Introduction

The ability to assemble nanocrystals (NCs) into structures with specific physical, chemical, optical or catalytic properties is a major goal of nanoscience and nanotechnology. Over the years, many different strategies have been successfully developed towards this goal. These include DNA assembly[1], electrostatic regulation[2], tectons[3], inter-polymer complexation[4] and many others[5].

Solvent Evaporation (SE)[5–7], where a solution containing stable NCs is slowly evaporated leading to assembled NC structures is among the most successful strategies. In a previous paper[8], we have described the dynamics of SE and characterized many aspects of the equilibrium clusters. It was also shown that the well known Maxwell theory of evaporation[9], which identifies the diffusion of vapor molecules as the slowest relaxation time, breaks down, as numerical results show a linear dependence of relaxation times with N, the number of NCs within the droplet.

The focus of this paper is the conceptual aspects of the problem, namely, a detailed classification of the equilibrium structures, particularly its relation to emergent icosahedral order[10] and the adequacy of available models to describe NC separations, the actual dependence of relaxation times with the number of NCs and the characterization of the physical processes that explain these dependencies. Molecular Dynamics (MD) will be conducted with octane, nonane or decane as solvents, which together with previous studies with toluene[8], enable to elucidate those effects that are specific to the solvent. A very important parameter in describing a NC is the hard sphere radius R_H, which, as discussed in Ref. [11], is defined by the Optimal Packing Model (OPM)[12] formula

$$R_H = R_c(1+3\xi\lambda)^{1/3} \quad (1)$$

where R_c is the core radius, $\lambda = \frac{L}{R_c}$ is the softness with L the maximum extended length of the ligand, and $\xi = \frac{\sigma}{\sigma_{Max}}$ is the dimensionless grafting density, i.e. the ratio of the actual σ to the maximum possible grafting density σ_{Max}.

Previous studies of assembly by solvent evaporation[13–19] have characterized generic Lennard-Jones (LJ) particles by SE. Insofar as NCs are described by quasi-hard spheres (with their effective radius following Eq. 1), considerations from these simpler models apply to NC structures as well. There are, however, quite a few relevant specific effects that are related to the flexible shell, i.e. the ligands, and therefore, cannot be captured by these generic models. Those include vortices[20–24], orientational order[25,26], solvent-ligand interactions[27,28], NC clusters[29–31], or effects related to the solid interface[32], just to name a few. This is the reason why in this paper we consider models where both the flexible igands and the solvent are described explicitly.

Furthermore, theoretical[10] and experimental studies[33], have revealed and inherent tendency of NCs to favour icosahedral order. It is also a goal for this paper to investigate to what degree icosahedral order is present already for small NC clusters as a first step to relate them to other more general studies of clusters in soft matter and other fields[34–36], as well as to general studies of nucleation in NCs[37].

Department of Physics & Astronomy and Ames Laboratory - USDOE, Iowa State University, Ames, IA 50011, USA; E-mail: trvsst@ameslab.gov

† Electronic Supplementary Information (ESI) available: [details of any supplementary information available should be included here]. See DOI: 10.1039/cXsm00000x/

2 Model and Simulation details

All simulations used HOOMD-Blue[38] with rigid body dynamics[39] and were implemented through HOODLT[40]. Simulations consist of a number of solvent molecules N_s specified by the average density, $\bar{\rho}$ defined as

$$\bar{\rho} = M_w \frac{N_s}{V} \ , \tag{2}$$

where M_w is the molecular weight of the solvent and V is the volume of the simulation box. Then, we vary the average density of the particles while maintaining the simulation box temperature and number of particles fixed. We start by identifying at which average density liquid-gas coexistence occurs. Then $\bar{\rho}$ is decreased by incrementally increasing the volume V keeping N,N_s constant. Thus, the process is described by a sequence of values

$$\{\bar{\rho}_i\}_{i=1\cdots M} \ , \bar{\rho}_{i+1} < \bar{\rho}_i \quad \text{and} \quad \{N^{Eq}_{v,i}\}_{i=1\cdots M} \ , N^{Eq}_{v,i} < N^{Eq}_{v,i+1} \ , N^{Eq}_{v,M} = N_s \tag{3}$$

where $N^{Eq}_{v,i}$ is the equilibrium number of solvent molecules in the vapor phase, defined so that after the last expansion, all solvent molecules are in the vapor, that is the solvent is fully evaporated, as depicted in Fig. 1. More specific details for the simulation are provided in the SI.

In this work, octane is the solvent more thoroughly investigated, but nonane and decane were considered in some cases. This solvent has internal degrees of freedom related to the flexibility of the monomers, contrary to toluene, a completely rigid molecule investigated in previous work[8].

For the cases where we include nanocrystals, we use the following nanocrystal specifications: L=17.22 Å, R_c=10.15 Å, σ=0.595 Å^2, σ_{Max}=0.666 Å^2, consistent with previous estimates[8,11]. More details of the nanocrystal simulations are outlined in Table 1.

Table 1 Table of all simulation parameters. N = number of nanocrystals. N_s = number of solvent molecules.

NC_{type}	N	N_s	time steps
$Au_{201}(SC_{12})_{80}$	2	800	25E6
$Au_{201}(SC_{12})_{80}$	4	1083	30E6
$Au_{201}(SC_{12})_{80}$	5	3936	40E6
$Au_{201}(SC_{12})_{80}$	6	1398	40E6
$Au_{201}(SC_{12})_{80}$	7	2195	45E6
$Au_{201}(SC_{12})_{80}$	8	2177	60E6
$Au_{201}(SC_{12})_{80}$	9	2610	60E6
$Au_{201}(SC_{12})_{80}$	10	2500	70E6
$Au_{201}(SC_{12})_{80}$	13	2536	75E6
$Au_{201}(SC_{12})_{80}$	15	2000	100E6
$Au_{201}(SC_{12})_{80}$	18	3500	120E6
$Au_{201}(SC_{12})_{80}$	21	5500	130E6
$Au_{201}(SC_{12})_{80}$	23	5500	120E6
$Au_{201}(SC_{12})_{80}$	25	6000	160E6
$Au_{201}(SC_{12})_{80}$	27	7000	160E6
$Au_{201}(SC_{12})_{80}$	28	7500	175E6
$Au_{201}(SC_{12})_{80}$	29	8000	195E6

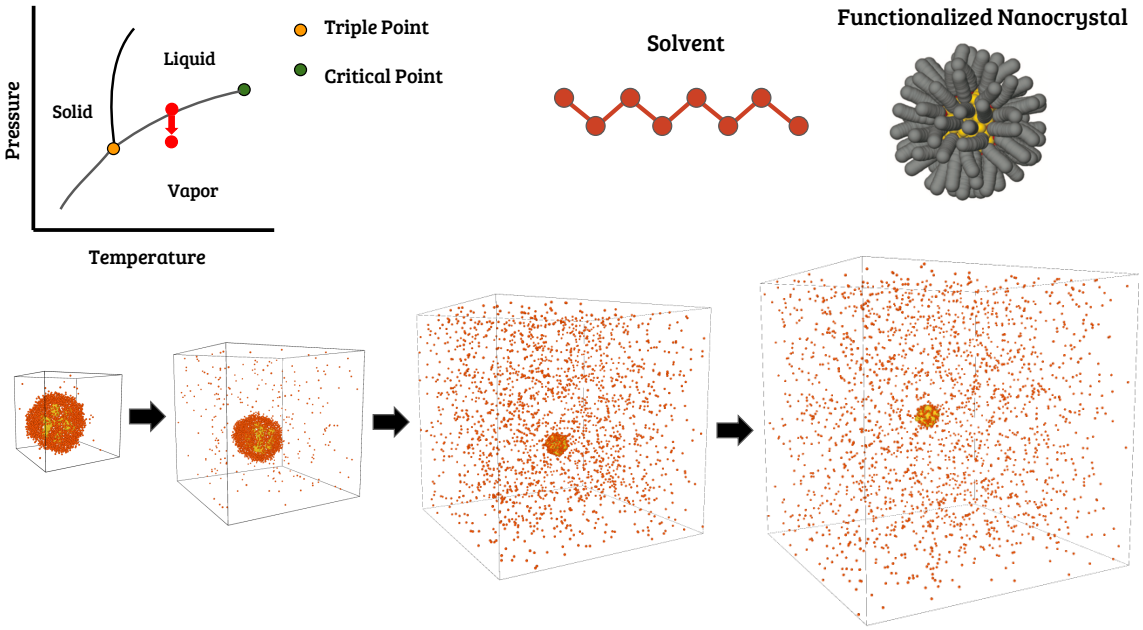

Fig. 1 Top left: Pressure vs Temperature phase diagram. After the liquid evaporates the solvent is entirely in the gas/vapor phase. Top right: Representation of the solvent (octane) and an alkylthiolated gold NC. Bottom: Example of the evaporation of a droplet containing $N = 13$ NCs.

3 Results

3.1 Pure Solvent

Density distributions for coexisting liquid and vapor, calculated as described in Ref.[41,42], are shown in Fig. 2. There is a bimodal distribution with two peaks representing equilibrium liquid and vapor densities. For octane, it is $\rho_l = 650(8)$ and $\rho_v = 2.7(5)$ (in kg/m^3), to be compared with experimental results $\rho_l^{exp} = 622.15$ and $\rho_v^{exp} = 2.705$, see Table **??**. For nonane it is $\rho_l = 669.87$ and $\rho_v = 2.164(9)$ (in kg/m^3) compared with $\rho_l^{exp} = 641.05(8)$ and $\rho_v^{exp} = 1.387(5)$, see Table **??**.

Following previous work[8], the pressure of the system is calculated from the ideal gas law from the expression

$$P = \rho_v \frac{RT}{M_w} , \tag{4}$$

which gives more accurate values than the actual pressure from the simulation, which shows large fluctuations due to the low density of the gas, and furthermore, becomes negative for sufficiently large liquid droplets, as shown in Fig. **??**.

The variation of the local density as a function of radial distance is shown in Fig. **??**. This was computed using RDF(Radial Distribution Function) from Python Freud library[43]. Since the local density is computed for a particle distance from a reference particle, we use the particle that is closest to the droplet center as the reference particle. We apply RDF to 1000 simulation frames and accumulate the results. From the accumulated results we identify three distinct regions. The first region is that to the left of the purple vertical bar, $r \leq R_{liquid}$, and has a mean density (slate-blue horizontal bar) equal to that computed for liquid particles using the method described in Fig. 2a. Likewise, the region to the right of the maroon vertical bar, $r \geq R_{liquid+interface}$, has a mean density (cyan horizontal bar) equal to that of vapor particles. The region, $R_{liquid} \leq r \leq R_{liquid+interface}$, is transitional between the liquid and vapor regions as we would expect from an interface. See Ref.[8].

3.2 NC Structures Upon Drying

3.2.1 Equilibrium clusters

We now analyze the structures obtained by evaporating a liquid droplet containing N NCs as described above, see also Fig. 1.

The first case is for a NC pair ($N = 2$). Once evaporation is complete, the results agree with previous estimates in dry conditions[22–24] and for toluene solvent[8], see Fig. **??** or Fig. **??** for example. Results for N=4,6,13 are shown in Fig. **??**, where the final structures are, respectively a tetrahedron, octahedron and icosahedron, which as shown in Fig. **??**, already emerge before full evaporation, with the final equilibrium distances agreeing with previous results obtained in dry conditions[22,24] and with toluene as solvent[8]. The equilibrium structure for N=10 corresponds to a Sphenocorona, see Fig. **??**. The N=13 forms a regular Icosahedron with a NC at its center, see Fig. **??**, which is in complete agreement with simulations with toluene[8]. Structures for other values of N are shown in Fig. **??**.

For $N > 21$, the structures are more complex and require further analysis. For N=23, see Fig. **??**, it corresponds to a pyramid with a trapezoid base while 4 adjacent hexagonal pyramids wrap around the vertically-central axis, forming the middle section of the structural surface. The Right of the figure shows how the hexagonal pyramids are joined by one of their edges. As for the bottom of the N=23 structure, one corner of each hexagonal pyramid is present such that they form the corners of a rhombus. The cores form the vertices of the stick-figure representation that is on the top left, similarly to the cases of Fig.s **??** and **??**.

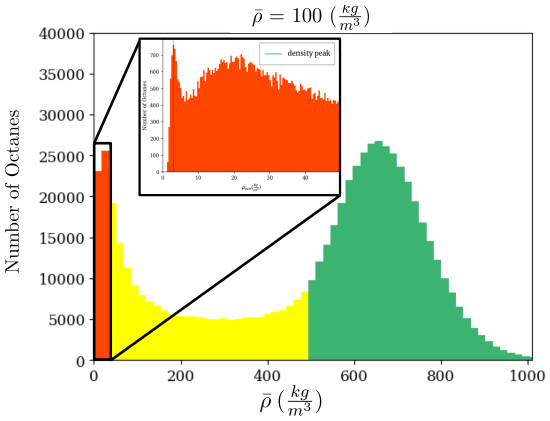

(a) Color-coded density distribution.

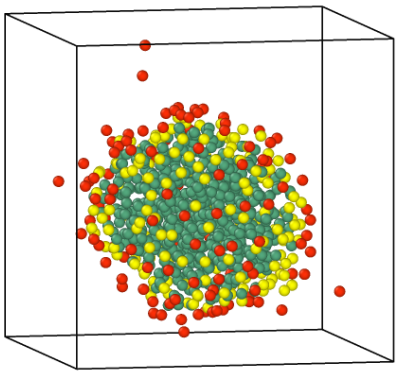

(b) Droplet snapshot.

Fig. 2 (a) Octane particle density distribution at $\bar{\rho} = 100\frac{kg}{m^3}$. The simulation was run for 1 million time steps and the data was stored in 999 time frames. The orange region corresponds to vapor particles, the yellow region corresponds to vapor and liq particles, and the green region corresponds to liquid particles. (b) The Octane droplet that corresponds to the density distribution that is in sub-Fig. a. The green is liquid, the yellow is liquid and vapor, and the orange is vapor. We approximate the droplet to be spherically symmetric.

Furthermore, two NCs are located inside the structure.

Similar analysis reveal the structures for N=25 (Fig. **??**), N=27 (Fig. **??**), N=28 (Fig. **??**) and N=29 (Fig. **??**).

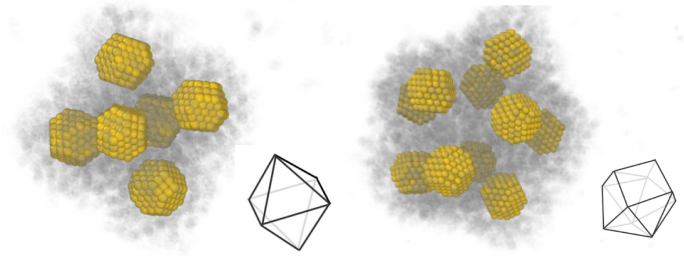

(a) N=6, Regular Octahedron

(b) N=10, Sphenocorona

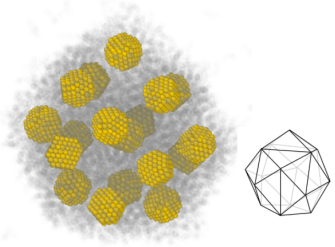

(c) N=18, Equatorially pentacapped axial bicapped pentagonal prism[44]

Fig. 3 Equilibrium structures: N=6, 10, 18.

Table 2 lists the NC-structure names for every given NC-number. Note that figures $N \geq 23$ remain unidentified. We have compared these structures with the Cambridge cluster database[45], see Fig. **??** and **??** for the different variants of the Lennard-Jones potential. We could not identify any of our clusters, with the most obvious difference being that the clusters in our study are defined by a surface where triangles appear as more equilateral.

Table 2 NC-number and corresponding structure name.

Number of NCs (N)	Structure name
4	Tetrahedron
5	Square pyramid
6	Regular Octahedron
7	Pentagonal Bipyramid
8	Biaugmented triangular prism
9	Gyroelongated Square pyramid
10	Sphenocorona
13	Icosahedron
15	Z_{14} Frank Kasper Phase
18	Equatorially pentacapped axial bicapped pentagonal prism[44]
21	Z_{20}
23	Unidentified
25	Unidentified
27	Unidentified
28	Unidentified
29	Unidentified

3.3 Characterization of inner NCs and vortices

For $N \geq 13$, the clusters contain inner NCs, i.e. those that are completely surrounded by other NCs. It is relevant to investigate their structures. This was done by averaging the NC configurations over several time frames and computing the Voronoi cell using the Voro++[46] software. The results are shown in Fig. 4 and 5 and were visually actualized using Mayavi, a python-written application.

In Fig. 6 we show some representative outer NC showing ligands that tilt away from their normals, i.e. vortices[20].

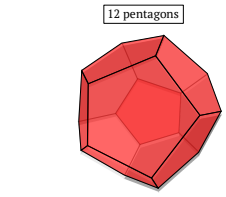

# edges	8	7	6	5	4	3
q=6-# edges	-2	-1	0	1	2	3
frequency	0	0	0	12	0	0

$\sum_{i=1}^{faces} q_i = 12$

(a) N=13

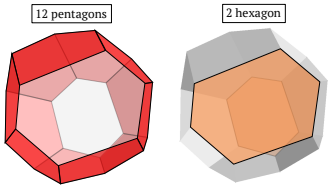

# edges	8	7	6	5	4	3
q=6-# edges	-2	-1	0	1	2	3
frequency	0	0	2	12	0	0

$\sum_{i=1}^{faces} q_i = 12$

(b) N=15

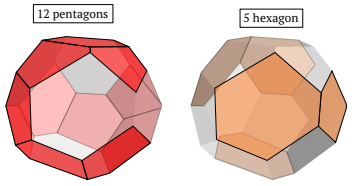

# edges	8	7	6	5	4	3
q=6-# edges	-2	-1	0	1	2	3
frequency	0	0	5	12	0	0

$\sum_{i=1}^{faces} q_i = 12$

(c) N=18

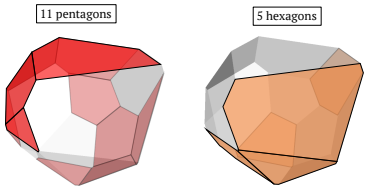

# edges	8	7	6	5	4	3
q=6-# edges	-2	-1	0	1	2	3
frequency	0	1	5	11	1	0

$\sum_{i=1}^{faces} q_i = 12$

(d) N=21

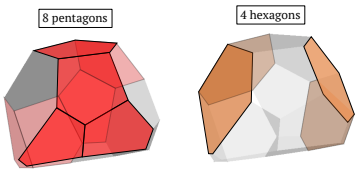

# edges	8	7	6	5	4	3
q=6-# edges	-2	-1	0	1	2	3
frequency	1	0	4	8	3	0

$\sum_{i=1}^{faces} q_i = 12$

(e) N=23, Inner particle 1

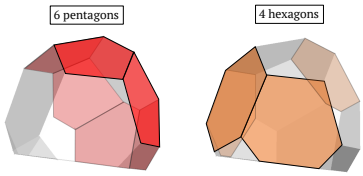

# edges	8	7	6	5	4	3
q=6-# edges	-2	-1	0	1	2	3
frequency	1	0	4	6	4	0

$\sum_{i=1}^{faces} q_i = 12$

(f) N=23, Inner particle 2

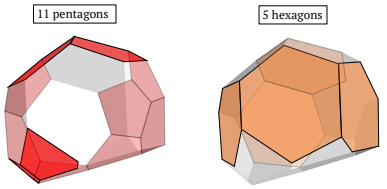

# edges	8	7	6	5	4	3
q=6-# edges	-2	-1	0	1	2	3
frequency	0	1	5	11	1	0

$\sum_{i=1}^{faces} q_i = 12$

(g) N=25, Inner particle 1

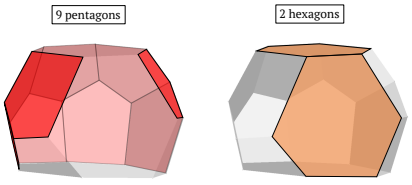

# edges	8	7	6	5	4	3
q=6-# edges	-2	-1	0	1	2	3
frequency	0	1	2	9	2	0

$\sum_{i=1}^{faces} q_i = 12$

(h) N=25, Inner particle 2

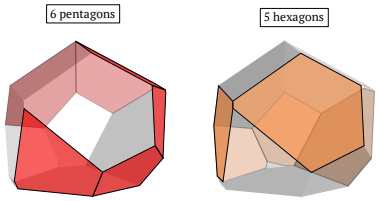

# edges	8	7	6	5	4	3
q=6-# edges	-2	-1	0	1	2	3
frequency	0	1	5	6	2	1

$\sum_{i=1}^{faces} q_i = 12$

(i) N=27, Inner particle 1

Fig. 4 Voronoi cells for inner NCs, I_N. Different NC-number, N, configurations have the following number of inner particles: N=13,15,18,21 have I_N=1; N=23,25 have I_N=2; N=27,28,29 have I_N=3.

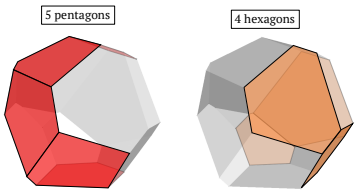

# edges	8	7	6	5	4	3
q=6-# edges	-2	-1	0	1	2	3
frequency	0	2	4	5	3	1

$\sum_{i=1}^{faces} q_i = 12$

(a) N=27, Inner particle 2

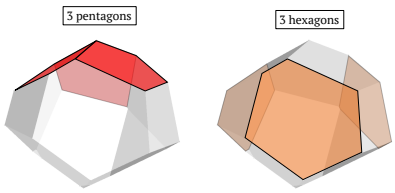

# edges	8	7	6	5	4	3
q=6-# edges	-2	-1	0	1	2	3
frequency	1	2	3	3	2	3

$\sum_{i=1}^{faces} q_i = 12$

(b) N=27, Inner particle 3

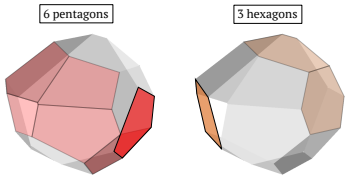

# edges	8	7	6	5	4	3
q=6-# edges	-2	-1	0	1	2	3
frequency	1	1	3	6	3	1

$\sum_{i=1}^{faces} q_i = 12$

(c) N=28, Inner particle 1

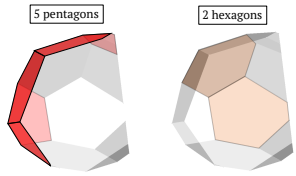

# edges	8	7	6	5	4	3
q=6-# edges	-2	-1	0	1	2	3
frequency	1	2	2	5	4	1

$\sum_{i=1}^{faces} q_i = 12$

(d) N=28, Inner particle 2

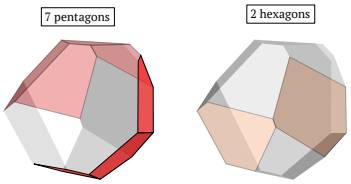

# edges	8	7	6	5	4	3
q=6-# edges	-2	-1	0	1	2	3
frequency	0	1	2	7	3	0

$\sum_{i=1}^{faces} q_i = 12$

(e) N=28, Inner particle 3

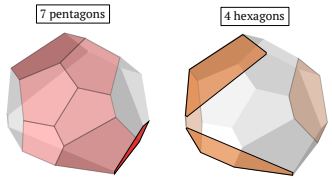

# edges	8	7	6	5	4	3
q=6-# edges	-2	-1	0	1	2	3
frequency	0	2	4	7	2	1

$\sum_{i=1}^{faces} q_i = 12$

(f) N=29, Inner particle 1

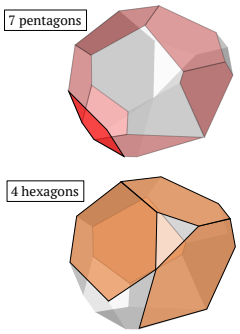

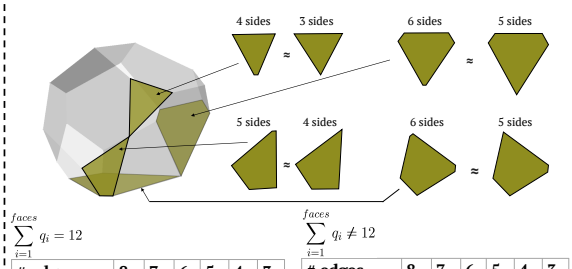

$\sum_{i=1}^{faces} q_i = 12$

# edges	8	7	6	5	4	3
q=6-# edges	-2	-1	0	1	2	3
frequency	0	0	6	6	3	0

$\approx$

$\sum_{i=1}^{faces} q_i \neq 12$

# edges	8	7	6	5	4	3
q=6-# edges	-2	-1	0	1	2	3
frequency	0	0	4	7	3	1

(g) N=29, Inner particle 2; Left: highlighted pentagons and hexagons. Right-top: describing how some face-edges were approximated to 0 length. Right-bottom: the edge-counting table.

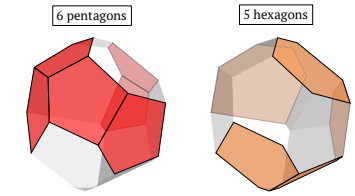

# edges	8	7	6	5	4	3
q=6-# edges	-2	-1	0	1	2	3
frequency	0	1	5	6	2	1

$\sum_{i=1}^{faces} q_i = 12$

(h) N=29, Inner particle 3

Fig. 5 Voronoi cells for inner NCs, I_N. Different NC-number, N, configurations have the following number of inner particles: N=13,15,18,21 have I_N=1; N=23,25 have I_N=2; N=27,28,29 have I_N=3.

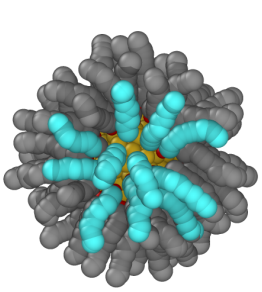

(a) N=13, icosahedron

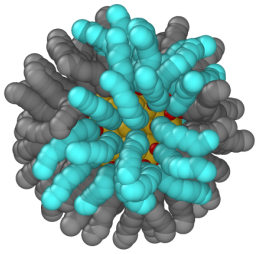

(b) N=15, Z_{14} Frank Kasper.

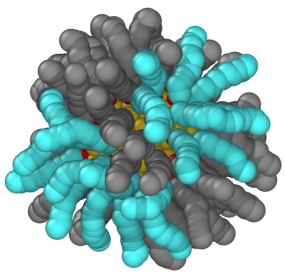

(c) N=18, Equatorially pentacapped ax-ial bi-capped pentagonal prism

Fig. 6 Representative vortices for the outer NC for (a) N=13 that (b) a N=15 (c) a N=18.

3.3.1 Droplet Radii

In Fig. 7a we show the evolution of the droplet radius as a function of $\bar{\rho}$. This radius is computed from the condition that the liquid and vapor have densities ρ_l, ρ_g respectively, see[8], and that the droplet contains NCs defined by its hard sphere radius R_H as defined by Eq. 1

$$R_d(\bar{\rho}) = \left(\frac{1 + \frac{4\pi\rho_l N}{3M_w N_s} R_{HS}^3 - \frac{\rho_g}{\bar{\rho}}}{\frac{4\pi}{3M_w}(\rho_l - \rho_g)} \right)^{1/3} N_s^{1/3} = \left(\frac{1 + \frac{N v_{NC}}{N_s v_l} - \frac{\rho_g}{\bar{\rho}}}{\frac{4\pi}{3M_w}(\rho_l - \rho_g)} \right)^{1/3} N_s^{1/3} \tag{5}$$

As shown in Fig. 7b the previous equation describes the simulation results with excellent precision.

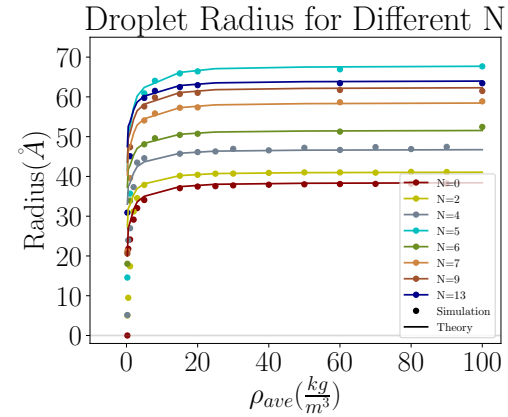

(a) Droplet Radii for different NC-number.

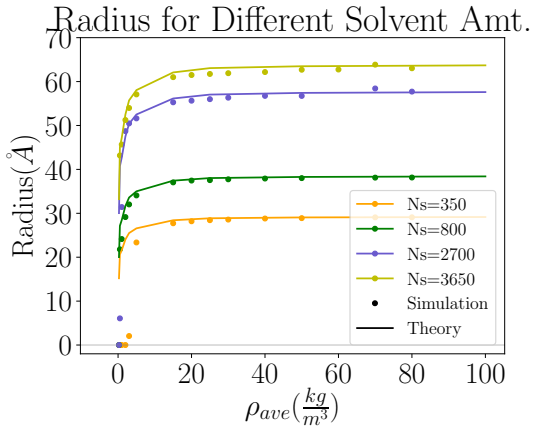

(b) Simulated vs theoretical droplet radii for different number,N, of Octane solvents.

Fig. 7 Droplet radius; theoretical vs simulation.

3.3.2 Relaxation times

The longest relaxation time τ_R is defined from

$$N_v(t) = N_{v,i}^{Eq} - (N_{v,i}^{Eq} - N_v(0))e^{-t/\tau_R} , \tag{6}$$

where $N_v(t)$ is the number of vapor solvent at any given time, and $N_{v,i}^{Eq}$ is the equilibrium value at the corresponding average density, see Eq. 3. Usually, $N_v(0) = N_{v,i-1}^{Eq}$. Note that τ_R also depends on the index i though the overall volume V and the size of the droplet. Eq. 6 is applicable at the latest stages of the equilibration process, where contributions from faster relaxation times have already vanished.

Fitting Eq. 6 to simulations, see Fig. **??**, we obtain τ_R for each value of N, shown in Fig. 8, where for small N the relaxation times grow linearly

$$\tau_R = \tau_r + \tau_0 N . \tag{7}$$

with $\tau_0 = 3.026$ ns. This is to be compared with the results for toluene, $\tau_0^{\text{toluene}} = 1.312$ ns[8]. For larger values of N, the growth of the relaxation times with N is sub-linear $\tau_R \propto N^{\beta}$. Results are consistent with $\beta = \frac{2}{3}$, but given the limited range in N, the range of acceptable β is broad.

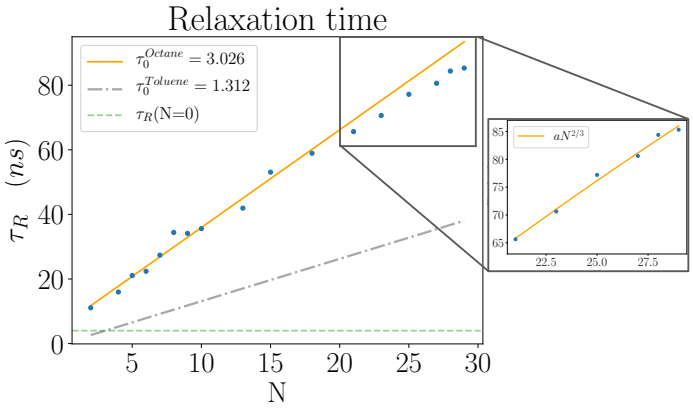

Fig. 8 Relaxation time vs N. For small N the data is linear, see Eq. 7 with $\tau_0 = 3.026$ ns. For larger N the data is consistent with $\tau_0 \propto N^{2/3}$, although other exponents provide satisfactory fits. Also shown is the $N = 0$ prediction given by Maxwell theory (green dashed), see Eq. 11, and previous results for toluene($\tau_R = 1$ ns)

We correlate the relaxation times to the packing fraction, which is defined through the hard sphere radius R_H, see Eq. 1, and the droplet radius R_d by

$$\eta_{HS} = \frac{\frac{4}{3}\pi N R_{HS}^3}{\frac{4}{3}\pi R_d^3} = N\left(\frac{R_{HS}}{R_d}\right)^3 . \tag{8}$$

The results are shown in Fig. 10a. These semi-quantitative figure illustrates a drastic increase of τ_R once $\eta_{HS} \approx \eta_{HS}^f = 0.49$, where $\eta_{HS}^f = 0.49$ is where the hard sphere freezing transition occurs.

4 Discussion

4.1 Analysis of NC Clusters

The ultimate goal of SE is the engineering of relevant structures, whether superlattices, quasi-crystals or complex clusters. In Ref.[10], it was shown that all BNSLs reported to date maybe understood as "frustrated icosahedral" assemblies, i.e. Quasi-Frank-Kasper[47] phases. If this is the case, NCs should exhibit a universal tendency towards icosahedral unit cells, already before crystal nucleation occurs. Experimental, see Ref.[33], and numerical evidence, see Ref.[24], has recently been reported supporting this conclusion.

Icosahedral order is reflected as a predominance of regular (or close to it) pentagons as faces of the Voronoi cell (of the inner

NCs) with some additional polygons (hexagons, heptagons, etc..) interpreted as disclinations[10,48]. Our equilibrated clusters, see Fig. 4,5, are entirely consistent with icosahedral order: There is an obvious predominance of pentagons, which tend to be regular or close to it, with distortions mostly due to the the small size of our clusters, which only allow between 1 and 3 inner NCs.

More concretely, The N=13 consists of 1 inner NC with a perfect dodecahedral cell containing just 12 pentagons. The other clusters with 1 interior NC (N=15-21) also conform to a dominance of pentagons, specially N=21, which was identified[10] as Z_{20}, a higher order Frank-Kasper[47] motif. The cases containing 2 interior NCs, $N = 23, 25$ are slightly less symmetric, which arises from the competition between the outer NCs, dominated by surface tension, but still show a majority of pentagons. The cases containing 3 NCs are more symmetric, see N=29 in Fig. 5.

4.2 Analysis of Vortices and NC distances

For the NCs used, the OPM prediction Eq. 1, gives a hard sphere NC radius

$$R_H = 17.9 \text{ Å} \tag{9}$$

Fig. 9 shows the half-distances between the inner and nearest neighbor NCs where we identified nearest neighbors NC through the faces of the Voronoi cells through Voro++[46]. In particular, we calculated the half-distances for cases where $N \geq 13$. The box plots are intended to illustrate the spread of halved-distances per NC configuration and show how they distribute near the value marked by the black dashed line given by Eq. 9.

As predicted by the OTM[20,21], given the large coordination of the inner NCs, their effective radius is described by Eq. 9. Note that for $N = 13$ the actual value , see Fig. 9, is slightly below the prediction, Eq. 9, as the radius of the outer NCs becomes smaller due to the presence of vortices[24], which are shown in Fig. 6. Additional vortices occurring on outer NCs with low coordination are also shown. We refer to previous publications[22,49] for more detailed studies on the structure of vortices.

4.3 Maxwell theory and relaxation times

The Maxwell theory describes droplet evaporation[9] as a process whose slowest relaxation time is determined by the diffusion of vapor molecules

$$\frac{\partial}{\partial t} n_v(\mathbf{r},t) = D^g \Delta n_v(\mathbf{r},t) \ , \tag{10}$$

where $n_v(\mathbf{r},t)$ is the vapor number density and D^g is the diffusion coefficient of the vapor molecules, given by $D^g = \frac{2k_BT}{3\pi d_s^2 P_c}\left(\frac{k_BT}{\pi m}\right)^{1/2}$. Eq. 10 implies a relaxation time

$$\tau_R \approx \frac{V^{2/3}}{D^g} \ . \tag{11}$$

For octane at T=387K, with P_c(387K) =0.878 atm, and d_s=8 Å, where P_c is the pressure of the vapor at the liquid-gas coexistence(see Fig. 2a) and d_s the octane gyration radius the relaxation time is

$$\tau_R \approx 4ns \ . \tag{12}$$

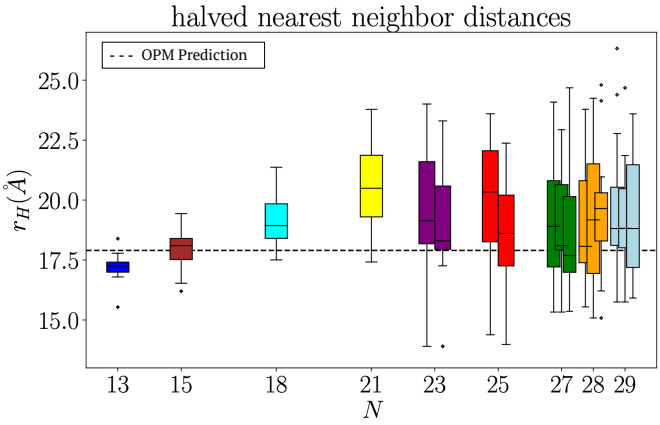

Fig. 9 Values of half the nearest neighbor distances, r_H, with respect to inner NC.

Thus, Eq. 11 is consistent with $N = 0$, see Fig. 8, and for finite N when $\eta_{HS} << \eta_{HS}^f$, see Fig. 10a, but clearly breaks down otherwise.

A different relaxation time $\tau_{R,l}$ is obtained by estimating the diffusion constant of the solvent within the liquid droplet (mostly dried as it contains the N NCs at high packing) from

$$\langle (r - r_0)^2 \rangle = 6D^l t \ . \tag{13}$$

Then, it is defined by

$$\tau_{R,l} \approx \frac{R_d^2}{D^l} \propto \frac{V_l^{2/3}}{D^l} \propto N^{2/3} \quad \text{for } \eta_{HS} > \eta_{HS}^f \ . \tag{14}$$

where V_l is the volume occupied by the droplet. The assumption that $V_l \propto N$ is only possible when the NCs are packed sufficiently close and hence it requires $\eta_{HS} > \eta_{HS}^f$.

Because of the limited values of N available, the evaluation of D^l is challenging, as shown in SI, Fig. **??**. Overall, the results clearly support, see Fig. 10b, the relation

$$\tau_R \approx \tau_{R,l} \quad \text{for } \eta_{HS} > \eta_{HS}^f \ . \tag{15}$$

showing that the breakdown of Maxwell theory occurs because the slowest relaxation time arises from the slow diffusion of the solvent molecules trapped within the NC cluster. The consistency of the $N^{2/3}$ relation for large N, as shown in Fig. 8 (see the inset), provides further evidence that Eq. 14 is the slowest relaxation time of the system.

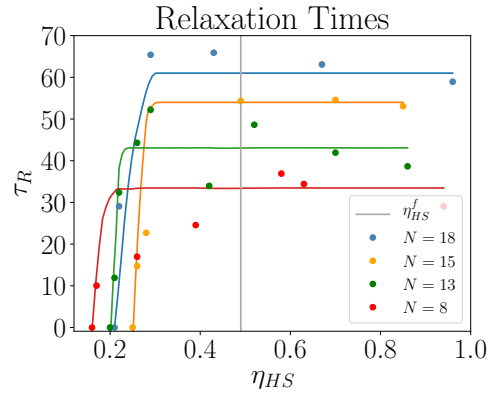

(a)

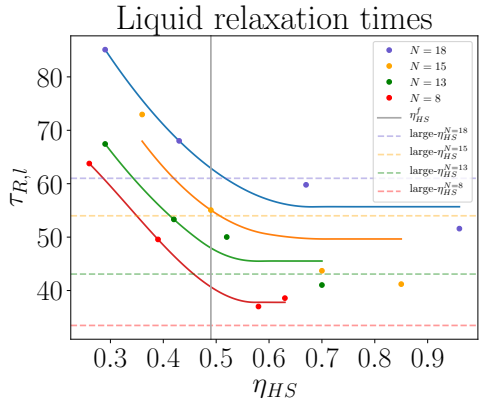

(b)

Fig. 10 Relaxation time from different-type fits. (a) from fits like those in Fig.s **??** and **??**. (b) from fitting solvent diffusion through (the close to dry) droplet.

5 Conclusions

We have presented a systematic investigation of the nanostructures obtained by solvent evaporation of N alkylthiolated NCs. The main results are the characterization of the different clusters as a function of N, Fig. **??**,**??**,**??** and Fig. 4,5 and the precise dependence of relaxation times, see Fig. 8, and the physical processes, fore example, the diffusion of solvent molecules within the cluster, see Eq.15.

The analysis of the NC clusters provides further evidence of the general tendency of NC towards icosahedral order, which is connected to putative glassiness [50] and provides some understanding on the stability of binary superlattices [10]. Recent experimental evidence, see Ref. [33], is in agreement with these results.

The analysis of the relaxation times is entirely consistent with a Maxwell regime Eq. 11, independent of N, dominated by the time for the vapor to diffuse away, and a new regime, dominated by the time for solvent molecules trapped within the cluster to finally escape to the vapor, which has a strong dependency on N, see Eq. 14, the number of NCs. The transition between the two regimes, see Fig. 10a, occurs at NC packing fraction (see Eq. 8) $\eta_{HS} \approx \eta^f_{HS} = 0.49$. In comparing our current results obtained with octane to previous studies with toluene [8], we obtain the same equilibrated clusters (when comparisons are available), yet toluene produces them more efficiently, as it has faster relaxation times, see Fig. 8. In any case, the agreement of the structures obtained by evaporation of different solvents is clearly indicative that equilibrium is achieved.

We have also shown, see Fig. 9 that the inner NCs (those that are surrounded entirely by other NCs), have effective hard sphere radius [11] entirely consistent with the OPM value, Eq. 1 and the appearance of vortices for the outer NCs, see Fig. 5. This provides further evidence on the validity of the Orbifold Topological Model (OTM) [20,21] to accurately describe nearest neighbor separation in general NC assemblies.

Other effects relevant for quantitative studies of evaporation include: effects related to the anchoring conditions of the droplet, Stefan flow, concentration changes at the droplet surface and temperature effects and [9]. By the choice of our system, we eliminated of all these effects: The first two are absent as droplets are freely suspended and there are no other gases present. The last two are also absent as our simulations are fully thermostated (differently from previous studies [14,17]) and therefore, prevent the development of temperature gradients.

The main limitation for our study is the small number of NCs ($N < 30$) considered. This is due to the considerable cost of including alkylthiolated ligands explicitly. We should emphasize that the relxation regime described by Eq. 14 is not possible to obtain with more coarse-grained models and therefore it seems challenging to extend our investigation to much larger values of N, which would be necessary in order to rigorously establish the $N^{2/3}$ regime apparent in Eq. 14 and Fig. 14. In that respect, recent density functional theories [51,52], may provide alternative approaches to this problem. Experimental results will be able to provide further clarification of these issues.

6 Supporting Information Available

- Table with all simulation parameters.
- Comparison of the pressure from the simulation (Virial, see Ref. [53]) and calculated from Eq. 4.
- Pressure as a function of average density.
- Phase coexistence as a function of average densities.
- Supplementary results for the droplet radius.
- Supplementary results for liquid diffusion.
- solvent evaporation plots and relaxation time fits.

acknowledgement

AT acknowledges many discussions and clarification of their work with I. Coropceanu and D. Talapin. Interest and discussions are also acknowledged from S. Mallapragada and D. Vaknin. The work is funded by NSF, DMR-CMMT 1606336 “CDS&E: Design Principles for Ordering Nanoparticles into Super-crystals”. This work used the Extreme Science and Engineering Discovery Environment (XSEDE), which is supported by National Science Foundation grant number ACI-1548562. Our project within XSEDE is supported by grant TG-MCB140071.

Notes and references

1 C. A. Mirkin, R. L. Letsinger, R. C. Mucic and J. J. Storhoff, *Nature*, 1996, **382**, 607–609.

2 H. Zhang, W. Wang, S. Mallapragada, A. Travesset and D. Vaknin, *Nanoscale*, 2017, **9**, 164–171.

3 P. J. Santos, Z. Cao, J. Zhang, A. Alexander-Katz and R. J. Macfarlane, *Journal of the American Chemical Society*, 2019, **141**, 14624–14632.

4 S. Nayak, N. Horst, H. Zhang, W. Wang, S. Mallapragada, A. Travesset and D. Vaknin, *Journal of Physical Chemistry C*, 2019, **123**, 836–840.

5 M. A. Boles, M. Engel and D. V. Talapin, *Chemical Reviews*, 2016, **116**, 11220–11289.

6 E. V. Shevchenko, D. V. Talapin, N. A. Kotov, S. O'Brien and C. B. Murray, *Nature*, 2006, **439**, 55–59.

7 M. A. Boles and D. V. Talapin, *Journal of the American Chemical Society*, 2015, **137**, 4494–4502.

8 T. Waltmannn and A. Travesset, *Nanoscale*, 2019, **11**, 18702–18714.

9 N. Fuchs, *Evaporation and Droplet Growth In Gaseous Media*, Pergamon Press, I edn, 1959, pp. 1–72.

10 A. Travesset, *Physical Review Letters*, 2017, **119**, 1–5.

11 X. Zha and A. Travesset, *Journal of Chemical Physics*, 2020, **152**, 094502.

12 U. Landman and W. D. Luedtke, *Faraday Discussions*, 2004, **125**, 1–22.

13 A. F. Routh and W. B. Zimmerman, *Chemical Engineering Science*, 2004, **59**, 2961–2968.

14 S. Cheng and G. S. Grest, *The Journal of Chemical Physics*, 2012, **136**, 214702.

15 S. Cheng and G. S. Grest, *Journal of Chemical Physics*, 2013, **138**, 64701.

16 M. Wang and J. F. Brady, *Soft Matter*, 2017, **13**, 8156–8170.

17 M. P. Howard, W. F. Reinhart, T. Sanyal, M. S. Shell, A. Nikoubashman and A. Z. Panagiotopoulos, *The Journal of Chemical Physics*, 2018, **149**, 094901.

18 M. P. Howard, A. Nikoubashman and A. Z. Panagiotopoulos, *Langmuir*, 2017, **33**, 3685–3693.

19 B. Chun, T. Yoo and H. W. Jung, *Soft Matter*, 2020, **16**, 523–533.

20 A. Travesset, *ACS Nano*, 2017, **11**, 5375–5382.

21 A. Travesset, *Soft Matter*, 2017, **13**, 147–157.

22 C. Waltmann, N. Horst and A. Travesset, *ACS Nano*, 2017, **11**, 11273–11282.

23 C. Waltmann, N. Horst and A. Travesset, *Journal of Chemical Physics*, 2018, **149**, 034109.

24 T. Waltmann, C. Waltmann, N. Horst and A. Travesset, *Journal of the American Chemical Society*, 2018, **140**, 8236–8245.

25 M. C. Weidman, D.-M. M. Smilgies and W. A. Tisdale, *Nature Materials*, 2016, **15**, 775–781.

26 Z. Fan and M. Grünwald, *Journal of the American Chemical Society*, 2019, **141**, 1980–1988.

27 D.-M. M. Smilgies and T. Hanrath, *EPL (Europhysics Letters)*, 2017, **119**, 28003.

28 I. Lokteva, M. Koof, M. Walther, G. Grübel and F. Lehmkühler, *Small*, 2019, **15**, 1900438.

29 A. Sánchez-Iglesias, M. Grzelczak, T. Altantzis, B. Goris, J. Pérez-Juste, S. Bals, G. Van Tendeloo, S. H. Donaldson, B. F. Chmelka, J. N. Israelachvili and L. M. Liz-Marzán, *ACS Nano*, 2012, **6**, 11059–11065.

30 J. E. Galván-Moya, T. Altantzis, K. Nelissen, F. M. Peeters, M. Grzelczak, L. M. Liz-Marzán, S. Bals and G. Van Tendeloo, *ACS Nano*, 2014, **8**, 3869–3875.

31 S. Merkens, M. Vakili, A. Sanchez-Iglesias, L. Litti, Y. Gao, P. V. Gwozdz, L. Sharpnack, R. H. Blick, L. M. Liz-Marzan, M. Grzelczak and M. Trebbin, *ACS Nano*, 2019, **13**, 6596–6604.

32 W. Liu, J. Midya, M. Kappl, H. J. Butt and A. Nikoubashman, *ACS Nano*, 2019, **13**, 4972–4979.

33 I. Coropceanu, M. A. Boles and D. V. Talapin, *Journal of the American Chemical Society*, 2019, **141**, 5728–5740.

34 D. Wales, *Energy Landscapes*, Cambridge University Press, 2003.

35 H. Kusumaatmaja and D. J. Wales, *Phys. Rev. Lett.*, 2013, **110**, 165502.

36 J. Wang, C. F. Mbah, T. Przybilla, B. Apeleo Zubiri, E. Spiecker, M. Engel and N. Vogel, *Nature Communications*, 2018, **9**, year.

37 S. Lee, E. G. Teich, M. Engel and S. C. Glotzer, *Proceedings of the National Academy of Sciences*, 2019, **116**, 14843–14851.

38 J. A. Anderson, C. D. Lorenz and A. Travesset, *Journal of Computational Physics*, 2008, **227**, 5342–5359.

39 J. Glaser, T. D. Nguyen, J. A. Anderson, P. Lui, F. Spiga, J. A. Millan, D. C. Morse and S. C. Glotzer, *Computer Physics Communications*, 2015, **192**, 97–107.

40 A. Travesset, *Journal of Chemical Physics*, 2014, **141**, 164501.

41 J. T. Fern, D. J. Keffer and W. V. Steele, *J. Phys. Chem. B*, 2007, **111**, 13278–13286.

42 J. T. Fern, D. J. Keffer and W. V. Steele, *J. Phys. Chem. B*, 2007, **111**, 3469–3475.

43 A. Haji-Akbari and S. C. Glotzer, *Journal of Physics A: Mathematical and Theoretical*, 2015, **48**, 485201.

44 R. Allmann, R. Hinek and A. Rühl Stephan, *Acta Cryst.*, 2010, p. 174.

45 D. J. Wales, J. P. K. Doye, M. P. H. A. Dullweber, F. Y. N. F. Calvo, J. Hernández-Rojas and T. F. Middleton, *The Cambridge Cluster Database*, `http://www-wales.ch.cam.ac.uk/CCD.html`.

46 C. Rycroft, *Chaos*, 2009, **19**, 41111.

47 F. C. Frank and J. S. Kasper, *Acta Crystallographica*, 1958, **11**, 184–190.

48 D. R. Nelson, *Physical Review B - Condensed Matter and Materials Physics*, 1983, **28**, 5515–5535.

49 X. Zha and A. Travesset, *Journal of Physical Chemistry C*, 2018, **122**, 23153–23164.

50 D. R. Nelson and M. Widom, *Nuclear Physics B*, 1984, **240**, 113–139.

51 V. V. Ginzburg, *Macromolecules*, 2017, **50**, 9445–9455.
52 L. L. Missoni and M. Tagliazucchi, *ACS Nano*, 2020, acsnano.0c00076.
53 J. Glaser, X. Zha, J. A. Anderson, S. C. Glotzer and A. Travesset, *Computational Materials Science*, 2020, **173**, 109430.